Internal droplet circulation induced by surface-driven rotation

Constantine M. Megaridis,* Joseph T. Hodges,† Jun Xin,*Joseph M. Day* and Cary Presser†

* Department of Mechanical Engineering, The University of Illinois at Chicago, Chicago, IL, USA

† National Institute of Standards and Technology, Gaithersburg, MD, USA

This paper presents a combined theoretical/experimental study of internal liquid circulation induced by droplet surface rotation. A numerical model is presented first, examining the fluid transport within a spherical liquid volume whose surface is subjected to rotation about a central axis. The model predicts that the steady-state motion established from spatially nonuniform surface rotation has a helical character and bears little resemblance to the toroidal internal flows developed within droplets under axisymmetric conditions. Similar internal flow patterns are predicted for temporally varying surface rotation occurring during droplet spin-up or spin-down. Planar laser-induced fluorescence is employed to provide high-resolution images of fluid flow developed within millimeter-sized suspended droplets that are exposed to steady laminar air streams to induce repeatable surface rotation. The predicted spiral flow patterns are corroborated by the pendant droplet visualization experiments, and suggest that nonuniform rotation or transient spinning may significantly alter internal droplet dynamics.

Keywords: droplet; circulation; rotation

1. Introduction

Droplet phenomena are relevant to a wide variety of physical processes ranging from atmospheric transport of rain droplets to spray cooling and liquid–fuel evaporation and combustion. Most of these phenomena involve situations where the droplets have a relative translational velocity with respect to the surrounding gaseous medium. The shear interaction of the two phases across the gas–liquid interface frequently establishes droplet internal motion (Hill 1894). In nonisothermal flows, droplet internal circulation can also be developed because of interfacial temperature gradients (Lozinski and Matalon 1993). The fluid motion within liquid droplets is of great importance for practical applications involving droplet transport. For example, liquid circulation in a fuel droplet enhances both heat and mass transport, thus affecting the relevant mixing, evaporation, and combustion rates (see review articles by Law 1982; Faeth 1983; Sirignano 1983; Dwyer 1989). Internal circulation can also impact the drag force exerted by the host medium on the droplet, and in so doing, affect the bulk motion. It is therefore evident that, in order to enhance our current understanding of droplet-related processes, it is necessary to adequately characterize the droplet internal motion and determine its overall influence on spray dynamics.

The fundamental mode of internal motion within a droplet was described a century ago by Hill (1894). It was shown that an axisymmetric vortex structure (known as Hill's vortex) can satisfy the equations of continuity and momentum within a spheroidal droplet. It was later postulated that such an internal flow could be induced by exposing a droplet to a steady laminar axisymmetric fluid flow. The basic hydrodynamics of the flow (both internal and external to a droplet) were solved by Hadamard (1911) and Rybczinski (1911). These analyses considered creeping viscous flows past liquid spheres. Just after the middle of this century and spanning over 20 years, several investigators (Spells 1952; Garner 1954; Kintner et al. 1961; Horton et al. 1965; Pruppacher and Beard 1970; Dayal et al. 1971; Sarma and Mondal 1975) visualized Hill's vortices in millimeter-sized droplets using a number of experimental configurations. These studies, which included both liquid and gaseous media, proved beyond doubt that toroidal internal circulation can occur in droplets having a relative velocity with respect to the host medium. However, these measurements were generally too qualitative to provide sufficiently detailed data for model validation.

The effect of internal motion on rates of mass transport for small droplets was initially believed to be insignificant, although it was predicted by Harriott (1962) that (for a sufficiently high droplet Reynolds number) mass transfer coefficients of circulating droplets could be as much as two and a half times greater than those of quiescent droplets. Indeed, the importance of internal circulation has become increasingly apparent with time. The aerodynamics of internal circulation in large, free-falling, deformable, nonevaporating water droplets were initially addressed by McDonald (1954). LeClair et al. (1972) used seed particles and streak photography to obtain data on the particle trajectories and to estimate average liquid velocities inside droplets suspended in laminar air

Address reprint requests to Professor Megaridis at the Department of Mechanical Engineering (M/C 251), University of Illinois at Chicago, 842, W. Taylor St., Chicago, IL 60607-7022, USA.

Received 1 January 1994; accepted 22 May 1994

streams. Since the flow patterns were visualized inside droplets that were highly loaded with seed particles, there was some ambiguity in the results regarding the unknown influence of such large populations of solid tracers on the induced liquid motion.

More recently, Winter and Melton (1990) utilized oxygen quenching of laser-induced fluorescence from naphthalene to examine the significance of internal circulation within sub-millimeter hydrocarbon droplets at room temperature. The fluorescing droplets studied by Winter and Melton were illuminated with a laser sheet and photographed. The spatial distribution of fluorescent intensity was dependent upon the local oxygen concentration and thus indirectly revealed patterns of internal circulation within the droplets. The authors stated that the liquid circulation may have been influenced (to a questionable degree) by the process of droplet injection. In that study, liquid-component vaporization was suppressed due to the nature of the liquid component (decane) used in that work and the room-temperature experimental conditions.

In a subsequent study, Winter (1993) used different droplet-generation techniques to unambiguously determine the source of internal circulation of droplets falling a short distance in a chamber filled with a shear flow of nitrogen and a variable amount of oxygen. These measurements provided internal flow patterns that occasionally revealed signs of droplet spin. No direct comparisons with numerical models of internal circulation were made.

Another recent experimental study by Wong and Lin (1992) provided indirect evidence of toroidal shear-induced circulation in the interior of large, hydrocarbon droplets that were exposed to high-temperature gaseous streams at atmospheric pressure. The JP-10 and decane droplets studied by Wong and Lin had an initial diameter of 2 mm, and were suspended using a thin shell-shaped probe specially designed to minimize interference with the internal liquid motion. It is important to note, however, that Wong and Lin deduced results on internal droplet dynamics from transient internal temperature distributions.

The mechanism of internal liquid circulation has been included in several detailed droplet evaporation models that were developed over the past decade (Prakash and Sirignano 1980; Renksizbulut and Haywood 1988; Haywood et al. 1989; Yung et al. 1991; Chiang et al. 1992). These models examined isolated nondeforming droplets exposed to axisymmetric, laminar, convective flows, and predicted the occurrence of two-dimensional (2-D) toroidal internal circulation patterns—similar to Hill's vortices—at sufficiently high droplet Reynolds numbers. Slightly distorted but similar flow patterns were reported by Dandy and Leal (1989) for deformable non-evaporating droplets at intermediate Reynolds numbers. On the other hand, the comparatively slow development of quantitative diagnostic techniques has produced very little experimental data for validation of such models. At present, there exists only a few studies (see, for example, Megaridis 1993) that compare model predictions with transient, spatially resolved experimental field measurements in well-defined droplet flow systems.

The exposure of a solid sphere to a shear flow has been known to generate rotational motion with respect to its own axis. Eichhorn and Small (1964) used a Poiseuille flow to levitate hydrodynamically millimeter-size spheres within an inclined glass tube. When flow Reynolds numbers ranged from 80 to 250, steady angular velocities up to $34\,s^{-1}$ were consistently observed. Liquid droplets can also acquire an angular velocity around their own axis, as a result of atomizer design and/or turbulence vorticity. Natarajan (1974) observed the smoky wake of burning n-pentane droplets and reported evidence of droplet spinning. Rigid body droplet rotation and its effect on droplet evaporation has been theoretically examined by Lozinski and Matalon (1992) in the limit of small Reynolds and Marangoni numbers. No translational motion between droplet and ambient gas was considered in that study. Pearlman and Sohrab (1991) used a rotating fiber to induce droplet angular velocities up to 40 rps for millimeter-sized droplets suspended at the tip of the fiber. The droplet rotation in that configuration, however, was produced by the shear interaction between fiber and liquid, and was thus initiated from the droplet axis.

The objective of the current investigation is to characterize droplet internal flows induced by temporally varying or spatially nonuniform droplet-surface rotation, either of which may develop when a droplet encounters a shearing flow, or a locally rotating gaseous field (a turbulent eddy, for example, where a droplet is instantaneously located), or perhaps by the angular momentum imparted to a droplet during spray atomization. This rotation may also be a result of the torque experienced by droplets in the dense spray limit (Kim et al. 1993). It should be noted that the liquid motion examined herein is not equivalent to the steady, rigid-body droplet rotation (spinning) that was theoretically addressed by Lozinski and Matalon (1992; 1993), or the fiber-induced droplet rotation investigated by Pearlman and Sohrab (1991).

A numerical model is presented below to predict the transient internal flows developed when specific modes of rotation are imposed upon the droplet surface. Subsequently, an experimental setup is described, featuring a flow configuration that

Notation

f_s	Droplet surface rotation frequency
p	Dimensionless pressure; normalized with respect to $\rho(\omega R)^2$
r	Dimensionless radial coordinate; normalized with respect to R
R	Droplet radius
t	Dimensionless time; normalized with respect to $1/\omega$
u	Dimensionless radial velocity component; normalized with respect to ωR
v	Dimensionless polar velocity component; normalized with respect to ωR
$\vec{V}$	Velocity vector
w	Dimensionless azimuthal velocity component; normalized with respect to ωR
x, y, z	Cartesian coordinates

Greek symbols

θ	Polar coordinate
ν	Liquid kinematic viscosity
ρ	Liquid density
φ	Azimuthal coordinate
ω	Reference angular velocity

Superscripts

n	Time level
T	Intermediate time level

has been specifically designed to induce droplet-surface rotation. Planar laser-induced fluorescence is employed to provide high resolution images of the flow patterns developed within millimeter-sized pendant water droplets exposed to steady laminar air streams. The visualized shear-induced droplet circulation is then combined with the predictions of the numerical model to produce a physical interpretation of the observed flow patterns.

2. Numerical model

Many practical situations of interest involve laminar droplet flows. In spray combustion applications, for example, the Reynolds number (based on droplet diameter) rarely exceeds values of the order of 100 (Sirignano 1993). The corresponding Reynolds numbers of free-falling rain droplets may be slightly higher, especially for the largest droplets. A detailed simulation of such flows will thus require the solution of the full Navier–Stokes equations in both the liquid and gas phases, with appropriate boundary conditions at the gas/liquid interface.

When liquid droplets encounter a locally rotating or nonuniform ambient flow, it is naturally expected that the droplet surface will first be affected through gas–liquid shear interaction. The droplet interior will subsequently adjust to the kinematic conditions imposed on the droplet surface. The current model examines the liquid isothermal flow within a spherical volume, whose surface is rotated around the z-axis passing through its center (see Figure 1). Since droplet surface rotation is generally time dependent, an unsteady formulation is adopted. The appropriate spherical coordinate system (r, θ, φ) is also shown in Figure 1, along with the respective velocity components (u, v, w). It should be noted that, even though the angular velocity ω may be φ-dependent, such a consideration would necessitate a three-dimensional (3-D) modeling approach, which is deemed to be out of the scope of the current work. To this end, a φ-independent ω is assumed. In summary, the model is characterized by

(1) symmetry with respect to the x–y (equatorial) plane (this implies that only half of the droplet volume (on either side of the x–y plane) needs to be modeled, and that the fluid motion in the symmetry plane is two-dimensional (2-D)); and
(2) symmetry with respect to the azimuthal coordinate φ about the z-axis (this condition simplifies the calculation considerably, since the droplet internal field needs to be determined only on a constant φ plane).

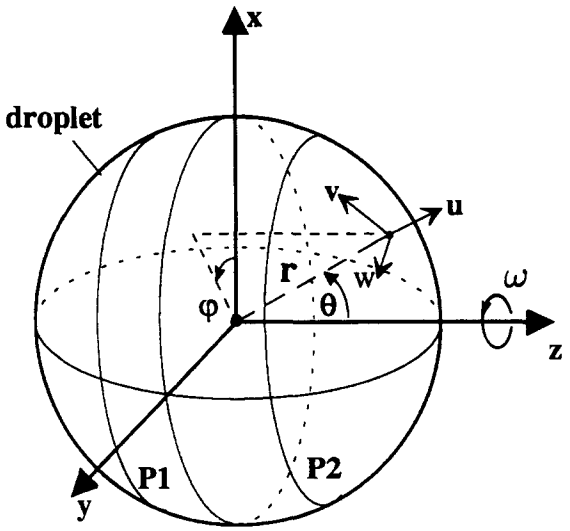

Figure 1 Droplet model configuration along with the relevant spherical coordinate system (r, θ, φ), and the respective velocity components (u, v, w)

The aforementioned symmetries thus effectively reduce the computational domain to a quarter-circle. The following assumptions are also adopted in our analysis:

(1) the droplet remains spherical (low Weber number flow);
(2) no liquid vaporization occurs;
(3) gravitational effects can be neglected; and
(4) fluid properties are constant.

Based on these assumptions, the *nondimensional* governing equations for a spherical coordinate system (Figure 1) are given below. In the following, ν denotes the kinematic viscosity of the liquid, ρ the liquid density, and R the droplet radius. If ω is a characteristic angular velocity representing the rotation of the droplet surface, the time has been normalized with respect to $1/\omega$, the velocities with respect to ωR, the radial coordinate with respect to R, and the pressure with respect to $\rho(\omega R)^2$.

Continuity equation

$$\frac{1}{r^2}\frac{\partial(r^2u)}{\partial r} + \frac{1}{r\sin\theta}\frac{\partial}{\partial\theta}(v\sin\theta) = 0 \tag{1}$$

Radial momentum equation

$$\frac{\partial u}{\partial t} + u\frac{\partial u}{\partial r} + \frac{v}{r}\frac{\partial u}{\partial\theta} - \frac{w^2+v^2}{r} = -\frac{\partial p}{\partial r} + \frac{\nu}{\omega R^2}\frac{1}{r^2}\left[\frac{\partial}{\partial r}\left(r^2\frac{\partial u}{\partial r}\right) + \frac{1}{\sin\theta}\frac{\partial}{\partial\theta}\left(\sin\theta\frac{\partial u}{\partial\theta}\right) - 2u - 2\frac{\partial v}{\partial\theta} - 2v\cot\theta\right] \tag{2}$$

Polar momentum equation

$$\frac{\partial v}{\partial t} + u\frac{\partial v}{\partial r} + \frac{v}{r}\frac{\partial v}{\partial\theta} + \frac{1}{r}(uv - w^2\cot\theta) = -\frac{1}{r}\frac{\partial p}{\partial\theta} + \frac{\nu}{\omega R^2}\frac{1}{r^2} \times \left[\frac{\partial}{\partial r}\left(r^2\frac{\partial v}{\partial r}\right) + \frac{1}{\sin\theta}\frac{\partial}{\partial\theta}\left(\sin\theta\frac{\partial v}{\partial\theta}\right) + 2\frac{\partial u}{\partial\theta} - \frac{v}{\sin^2\theta}\right] \tag{3}$$

Azimuthal momentum equation

$$\frac{\partial w}{\partial t} + u\frac{\partial w}{\partial r} + \frac{v}{r}\frac{\partial w}{\partial\theta} + \frac{uw + vw\cot\theta}{r} = \frac{\nu}{\omega R^2}\frac{1}{r^2}\left[\frac{\partial}{\partial r}\left(r^2\frac{\partial w}{\partial r}\right) + \frac{1}{\sin\theta}\frac{\partial}{\partial\theta}\left(\sin\theta\frac{\partial w}{\partial\theta}\right) - \frac{w}{\sin^2\theta}\right] \tag{4}$$

2.1. Initial and boundary conditions

The liquid is assumed to be initially quiescent ($u = v = w = 0$). In addition, the pressure in the droplet interior is initially uniform (atmospheric plus surface tension pressure).

The droplet-surface boundary conditions were formulated to reflect a rotation around the z-axis:

$$w = w(\theta); \qquad r = 1,\ 0 \le \theta \le \frac{\pi}{2} \tag{5}$$

where $w(\theta)$ denotes the functional dependence of the azimuthal velocity component on the polar coordinate θ. For uniform surface rotation, $w(\theta) = \sin\theta$. Note that w is a nondimensional quantity.

A zero shear ($\tau_{r\theta} = 0$) condition along θ was considered for v:

$$\partial v/\partial r - v = 0; \qquad r = 1,\ 0 < \theta < \frac{\pi}{2} \tag{6}$$

The above condition is justified in flow situations where the azimuthal (circumferential) velocity dominates any secondary motion.

In addition,

$$u = 0; \qquad r = 1,\ 0 \le \theta \le \frac{\pi}{2} \tag{7}$$

The following symmetry conditions were employed:

$$\frac{\partial u}{\partial \theta} = 0 = v = w; \qquad \theta = 0,\ 0 < r < 1 \tag{8}$$

$$\frac{\partial u}{\partial \theta} = v = 0 = \frac{\partial w}{\partial \theta}; \qquad \theta = \pi/2,\ 0 < r < 1 \tag{9}$$

$$v = 0; \qquad r = 1,\ \theta = 0 \text{ or } \theta = \pi/2 \tag{10}$$

A zero-velocity condition was implemented at the droplet center ($r = 0$). An interface condition for the pressure ($\partial p/\partial r$) was calculated from the radial momentum equation just below the droplet surface. The relevant velocity terms were determined using the field data at the previous time step. Finally, the pressure along the straight edges of the computational domain ($\theta = 0,\ \pi/2$) was computed from $\partial p/\partial\theta = 0$ as being consistent with the above-listed velocity boundary conditions and the polar momentum equation on the droplet surface.

2.2. Numerical solution procedure

The solution procedure was implemented using the methods given by Ferziger (1977) and Dukowicz (1980). The system of governing equations was discretized spatially on a staggered mesh. Central finite differencing was employed for the diffusion terms, while upwind differentiation was employed for the convection terms. The time-splitting algorithm (Dukowicz 1980) was employed for temporal discretization. This technique expresses the radial and polar momentum equations as

$$\frac{\partial u}{\partial t} = -\frac{\partial p}{\partial r} + F_r(\vec{V}) \tag{11}$$

$$\frac{\partial v}{\partial t} = -\frac{1}{r}\frac{\partial p}{\partial \theta} + F_\theta(\vec{V}) \tag{12}$$

where $\vec{V}$ denotes the velocity vector, and F_r, F_θ represent all convective and viscous terms of the corresponding momentum equation. A first-order difference for the time derivative is used to advance the solution from the current step n to an intermediate level (superscript T):

$$\frac{u^T - u^n}{\Delta t} = -\frac{\partial p^n}{\partial r} + F_r^n(\vec{V}) \tag{13}$$

$$\frac{v^T - v^n}{\Delta t} = -\frac{1}{r}\frac{\partial p^n}{\partial \theta} + F_\theta^n(\vec{V}) \tag{14}$$

The intermediate-level velocity must be corrected so that the pressure field and velocity field at the next time step $(n+1)$ satisfy the momentum and continuity equations simultaneously. At that level, the discretized momentum and continuity equations are

$$\frac{u^{n+1} - u^n}{\Delta t} = -\frac{\partial p^{n+1}}{\partial r} + F_r^n(\vec{V}) \tag{15}$$

$$\frac{v^{n+1} - v^n}{\Delta t} = -\frac{1}{r}\frac{\partial p^{n+1}}{\partial \theta} + F_\theta^n(\vec{V}) \tag{16}$$

$$\frac{1}{r^2}\frac{\partial}{\partial r}(r^2 u^{n+1}) + \frac{1}{r\sin\theta}\frac{\partial}{\partial \theta}(v^{n+1}\sin\theta) = 0 \tag{17}$$

Combining the above equations, we obtain

$$\frac{u^{n+1} - u^T}{\Delta t} = -\frac{\partial p^{n+1}}{\partial r} + \frac{\partial p^n}{\partial r} \tag{18}$$

$$\frac{v^{n+1} - v^T}{\Delta t} = -\frac{1}{r}\frac{\partial p^{n+1}}{\partial \theta} + \frac{1}{r}\frac{\partial p^n}{\partial \theta} \tag{19}$$

When Equations 18 and 19 are substituted into Equation 17, we obtain an expression used to update the pressure field:

$$\nabla^2 p^{n+1} - \nabla^2 p^n = \frac{1}{\Delta t}\left[\frac{\partial}{\partial r}(r^2 u^T) + \frac{r}{\sin\theta}\frac{\partial}{\partial \theta}(v^T \sin\theta)\right] \tag{20}$$

The numerical solution procedure can thus be summarized by these steps:

(1) Equations 13 and 14 are used to calculate u^T, v^T, respectively;
(2) Equation 20 is employed to calculate p^{n+1}, and this Poisson equation is solved using the successive overrelaxation (SOR) method;
(3) the velocities u^{n+1}, v^{n+1} are corrected using Equations 18 and 19; and finally,
(4) since the azimuthal component of the momentum equation is independent of the pressure field, the corresponding velocity w^{n+1} is directly calculated from Equation 4.

The above steps describe one complete computational cycle. This procedure is advanced in time and repeated until steady state is reached. Finally, the full character of the fluid flow is reconstructed by effectively rotating the computational quarter-circle domain around the z-axis by 360°.

3. Model predictions

The model was first employed to investigate the motion induced in the interior of a 2 mm-diameter water droplet whose surface is rotated around the z-axis at a steady frequency $f_s = 3$ Hz. The corresponding Reynolds number based on droplet diameter, liquid properties, and maximum surface rotation velocity (ωR) is around 38. It should be noted that the above droplet size and surface rotation frequency were selected to be relevant to the experimental measurements presented in the following section.

Initially, the sensitivity of the model predictions to both the time step and numerical grid were examined. A grid of 16 (along r) × 20 (along θ) nodes along with a nondimensional time step of 10^{-4} proved to be adequate for both time-step and grid-independent results. Steady state was reached after approximately 4×10^4 time steps (~ 0.2 s). The computations were performed on a Cray Y-MP computer[1]; a typical run required approximately 10 CPU minutes.

The steady-state motion within a spherical volume whose surface rotates at a certain frequency is a rigid-body rotation

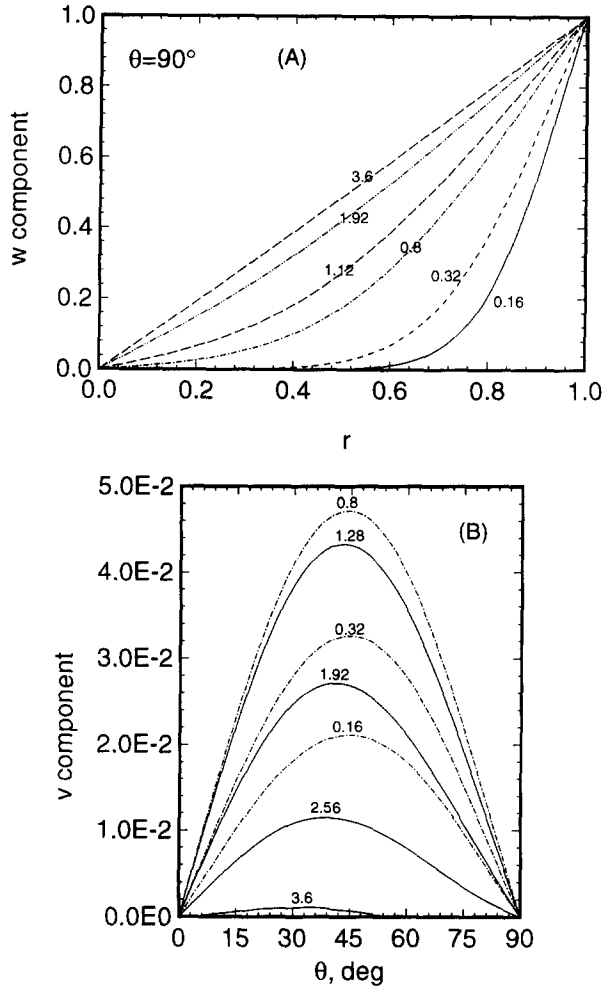

Figure 2 Model-predicted temporal profiles of the azimuthal (A) and polar (B) velocity components. The first are plotted as a function of the radial location along the x-axis ($\theta = 90°$), while the latter are shown with respect to the polar coordinate along the droplet surface

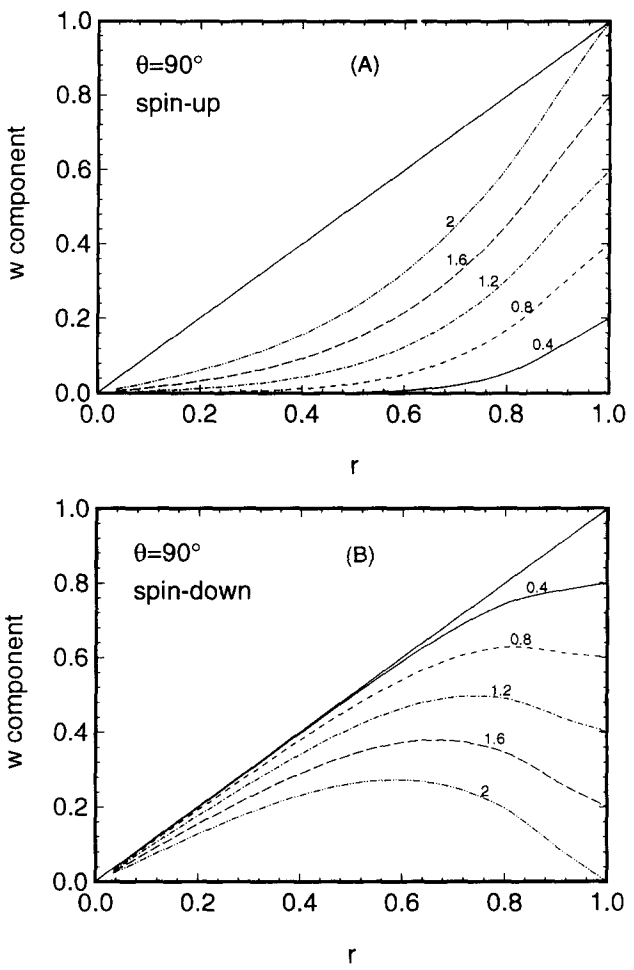

Figure 3 Temporal variation of azimuthal velocity radial distributions at $\theta = 90°$ for (A) droplet spin-up, and (B) droplet spin-down. The solid diagonal lines represent rigid body rotation

(Wimmer 1988). Figure 2 presents the model-predicted temporal profiles of the azimuthal (Figure 2A) and polar (Figure 2B) velocity components. The former are plotted as a function of the radial location along the x-axis ($\theta = 90°$), while the latter are shown with respect to the polar coordinate along the droplet surface. It is apparent that the transition from quiescence (time zero) to the rigid-body rotation is gradual and is almost complete approximately at nondimensional time 3.6 ($\sim$0.2 s). The temporal variation of the weak polar velocity component v (see Figure 2B) shows an interesting behavior; during the transient stage, and after the imposition of the surface rotation, this secondary velocity component achieves a temporal maximum at a nondimensional time of 0.8. It decreases steadily thereafter, until it eventually vanishes when the rigid-body motion is fully established.

The emergence of weak polar velocities during the transient stages of the development of rigid-body motion under steady surface rotation prompted two additional runs involving time-varying surface rotation. The first featured a linear increase of the surface rotation frequency from 0 Hz to 3 Hz between nondimensional time zero and two (spin-up). The second was characterized by a linear decrease of the surface rotation frequency from 3 Hz to 0 Hz between nondimensional times zero and two (spin-down from rigid-body motion). Figure 3 presents the temporal variation of the azimuthal velocity radial distributions at $\theta = 90°$. In the case of droplet spin-up (Figure 3A), the azimuthal velocity is initially zero (quiescent liquid) and gradually approaches the rigid-body motion with a frequency of 3 Hz, which is depicted by the straight diagonal line of Figure 3A. In the case of droplet spin-down (Figure 3B), the liquid motion increasingly deviates from the initial rigid-body rotation depicted by the straight diagonal line of Figure 3B.

Figure 4 presents the θ-dependence of the secondary polar velocity component on the droplet surface for both spin-up and spin-down runs. Even though the magnitude of v is comparable for the two runs, its direction depends on the accelerating or decelerating character of the liquid flow. As also reported by Wimmer (1988), during droplet spin-up the fluid on the droplet surface moves from the poles to the equator ($v > 0$), while during droplet spin-down the fluid on the droplet surface moves to the opposite direction ($v < 0$). Figure 5 presents the instantaneous x–z projections of the velocity vector fields for both spin-up (nondimensional time = 2) and spin-down (nondimensional time = 1.2) cases. It should be noted that the specific instance for the spin-down run corresponds to the most vigorous polar velocity profile (see Figure 4). Figure 5A shows that during spin-up the surface flow is directed from the poles to the equator; in the equator plane, the fluid moves towards

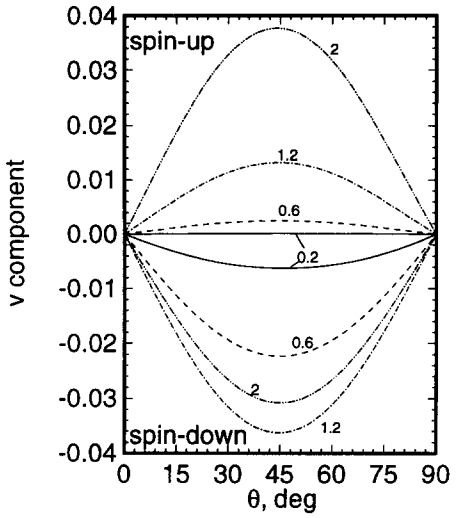

Figure 4 θ-dependence of the secondary polar velocity component on the droplet surface for both spin-up and spin-down runs

the center, and finally because of continuity it moves back to the poles. During droplet spin-down (Figure 5B), the surface fluid moves from the equator to the poles, and then to the droplet center before it turns outward again.

As seen so far, a uniform rotation imposed on the surface of a quiescent droplet triggers a short transient phase and eventually establishes a rigid-body motion. However, since

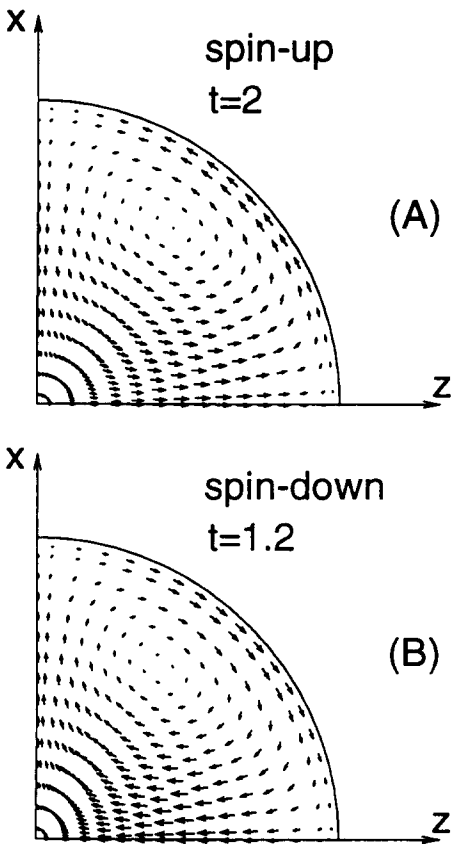

Figure 5 Instantaneous x–z projections of the velocity vector fields for (A) droplet spin-up (nondimensional time = 2), and (B) droplet spin-down (nondimensional time = 1.2)

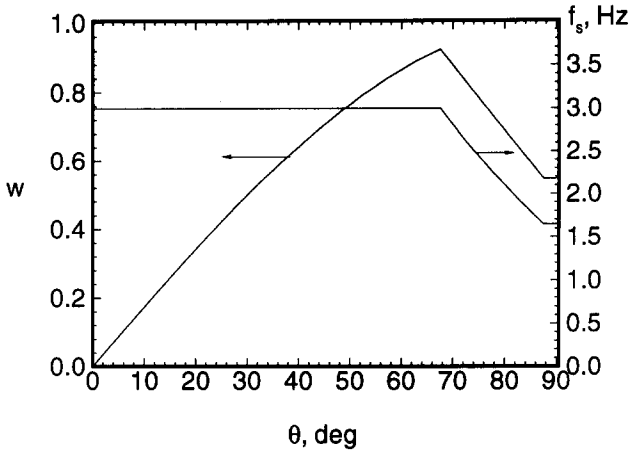

Figure 6 Polar variation of the surface rotation frequency f_s along with the corresponding azimuthal velocity w, chosen to simulate spatially nonuniform rotation conditions

non-uniform conditions have a much higher probability of occurring in practice, it is important to examine whether small deviations from uniform surface rotation give rise to non-rigid-body motion. Figure 6 presents the polar variation of the surface rotation frequency f_s along with the corresponding azimuthal velocity w, chosen to simulate nonuniform rotation conditions. This "ordered" non uniformity, although artificial and only along θ, represents an improvement over the more unlikely uniform rotation. The $\sin\theta$ dependence of w at $0° < \theta < 67.5°$ is due to the imposed uniform rotation (f_s = 3Hz) in that regime, while the declining values of f_s at $67.5° < \theta < 90°$ have been selected to give a linearly decreasing trend for w in that domain. In reference to the schematic of Figure 1, the surface conditions of Figure 6 reflect an obstructed droplet-surface circumferential motion between planes P1 and P2, both parallel to the x–y symmetry plane.

Figure 7 shows the predicted steady-state $v(\theta)$ profiles at five different radial distances from the droplet center (r = 0.68, 0.75, 0.82, 0.89, and 1) for the surface rotation conditions of Figure 6. The steady values of v on the droplet surface (r = 1) are comparable to the transient profiles depicted in Figure 2B. Figure 8 presents the variation of the dominant azimuthal velocity w along two droplet radii positioned at $\theta = 52.5°$ (Figure 8A) and 90° (Figure 8B), respectively. As seen, the values

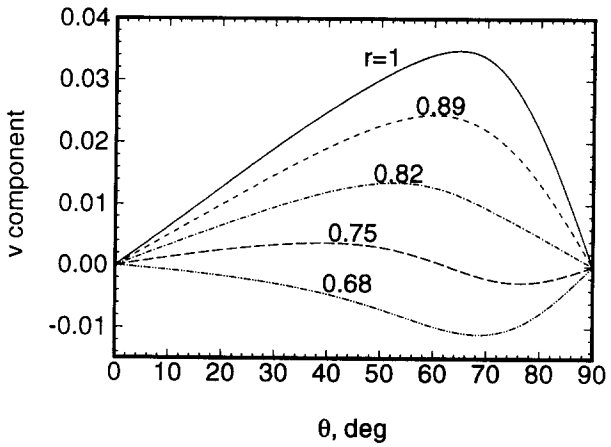

Figure 7 Model-predicted steady-state $v(\theta)$ profiles at five different radial distances from the droplet center for the surface rotation conditions of Figure 6

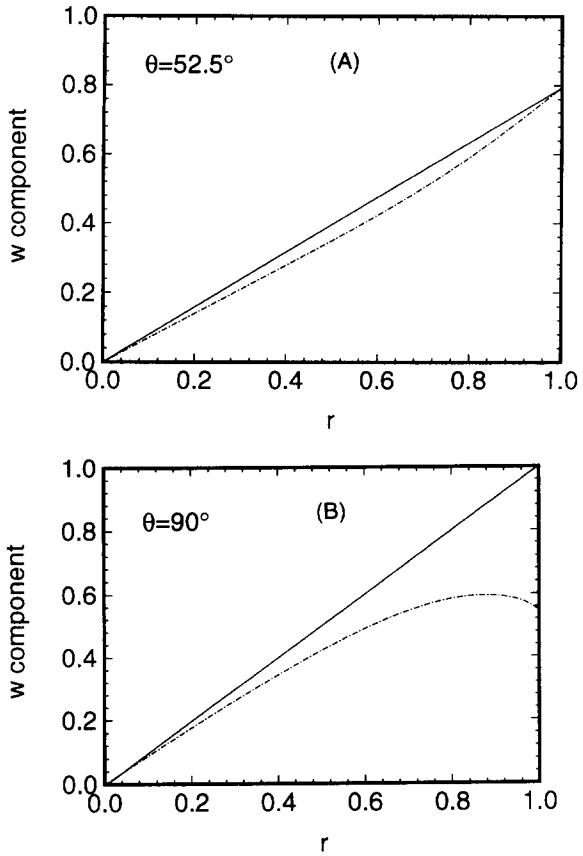

Figure 8 Model-predicted variation of azimuthal velocity component along two droplet radii positioned at (A) $\theta = 52.5°$, and (B) $\theta = 90°$. The solid lines correspond to rigid-body rotation

of w substantially lag those of a rigid-body rotation (solid lines). In addition, the influence of the imposed nonuniform rotation is much higher at $\theta = 90°$ than at $\theta = 52.5°$. A comparison of Figures 7 and 8 reveals that the magnitude of the polar velocity component v remains substantially smaller than the corresponding circumferential component w.

Figure 9 presents a typical trajectory of a flow-tracing element that is periodically transported in the vicinity of the droplet surface for the simulation characterized by the surface conditions shown in Figure 6. The time required for the completion of this trajectory is approximately 10 s. The entire path lies on the same side of the x–y plane, and has a complex three-dimensional (3-D) character. As shown in Figure 9, the fluid particle follows a spiraling motion away from the pole of the axis of rotation, while simultaneously moving closer to the equatorial (x–y) plane of symmetry with an almost constant value of radial distance from the droplet center ($r \sim 0.9$ for the path shown). After approaching the x–y plane, the fluid spirals inward from the equator to the droplet center, subsequently turns, and finally winds around the z-axis until it reaches its original position near the droplet surface. The same trajectory is repeated thereafter (steady-state motion). The particle movement from the pole to the equatorial plane results from the centrifugal force that tends to drive the particle away from the axis of rotation and hence in the direction of increasing polar angle (θ). It should be noted that the trajectory shown in Figure 9 is very different from typical trajectories within droplets exposed to axisymmetric flows. Therefore, it is apparent that the characteristic length scales of fluid transport in the interior of droplets whose surface is subjected to

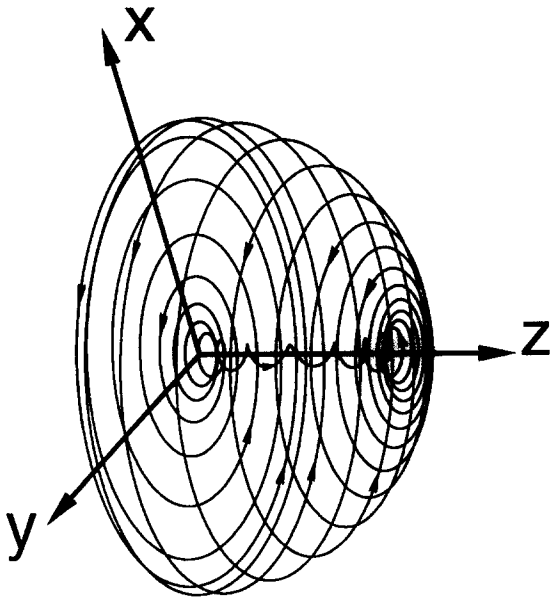

Figure 9 Typical trajectory of a flow-tracing element that is periodically transported in the vicinity of the droplet surface. Note the distinct difference from the toroidal trajectories established within droplets exposed to axisymmetric flows

nonuniform rotation are different than those established in toroidal recirculation flows within droplets.

Figures 10A and 10B, produced by the numerical model for the surface rotation conditions shown in Figure 6, represent characteristic projected views of the complex flow field within the droplet. Figure 10A presents a flow-tracing particle path within the symmetry (x–y) plane shown in Figure 1. This trajectory indicates that the fluid is convected in a spiral fashion towards the droplet center, before it turns away from the x–y plane in a direction parallel to the axis of rotation (Figure 9). Figure 10B presents a set of pseudo-streamlines (upper half) and velocity vectors (lower half) of the droplet secondary motion on a constant-φ plane, as attributed *only* to the radial (u) and polar (v) components of the liquid velocity field. The term pseudo-streamlines is used herein to denote that the rotational velocity component is not reflected in this representation. The composite internal motion consists of the well defined double toroidal circulation shown in Figure 10B, superimposed on the rotational component around the z-axis. The similarity between the toroidal flow pattern shown in Figure 10B and that depicted in Figure 24 of Wimmer (1988) is worth noting. However, the secondary motions compared are due to entirely different mechanisms (spatial vs. temporal nonuniformity of surface rotation). In addition, the secondary flow pattern of Figure 10B is very similar to that depicted in Figure 4 of Lozinski and Matalon (1993). However, the qualitatively similar motion reported in that work is due to thermocapillary forces established on the nonisothermal surface of a droplet rotated in a rigid-body fashion.

Similar trends regarding deviations from rigid-body uniform motion were also obtained when different nonuniform modes of surface rotation were utilized. To this end, the model predictions consistently show that helical droplet internal flows appear not only temporarily during the transient phases of spatially uniform, surface-driven rotation, but may also occur at steady state as a result of spatial nonuniformities along the polar coordinate. The following section describes an experimental setup used to produce nonuniform droplet surface rotation.

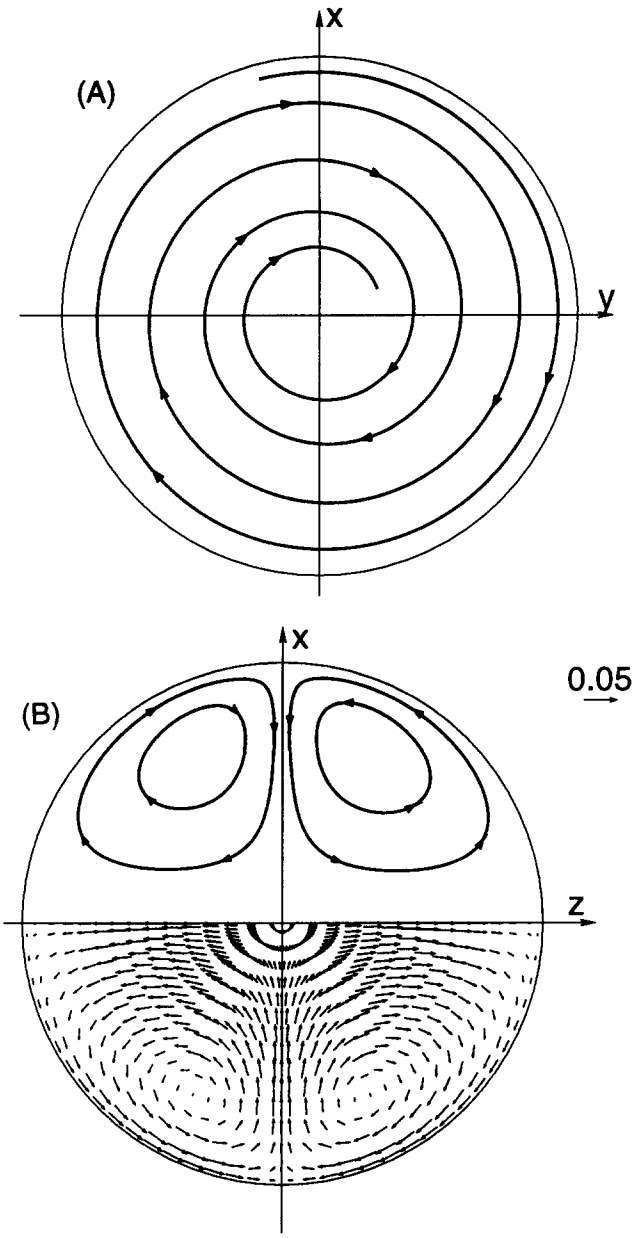

Figure 10 (A) Section of a numerically-predicted trajectory of a flow-tracing element within the symmetry (x–y) plane of the droplet. (B) Pseudo-streamlines (upper half) and velocity vectors (lower half) of the droplet secondary motion on a constant-φ plane, as attributed to the radial (u) and polar (v) components of the liquid velocity field

4. Flow visualization experiments

The experimental apparatus described below features water droplets suspended on a vertical, flat-tipped hypodermic needle. As depicted in the schematic of Figure 11, the droplet surface was observed to rotate at a steady angular velocity $\omega = d\varphi/dt$ with respect to the z-axis (Figure 1), after exposure to a uniform gas stream directed perpendicular to the needle/droplet vertical axis. The droplet surface rotation is attributed to the presence of the needle at the top of the droplet. The needle obstructs the gaseous flow in its vicinity, and consequently allows relatively little momentum exchange

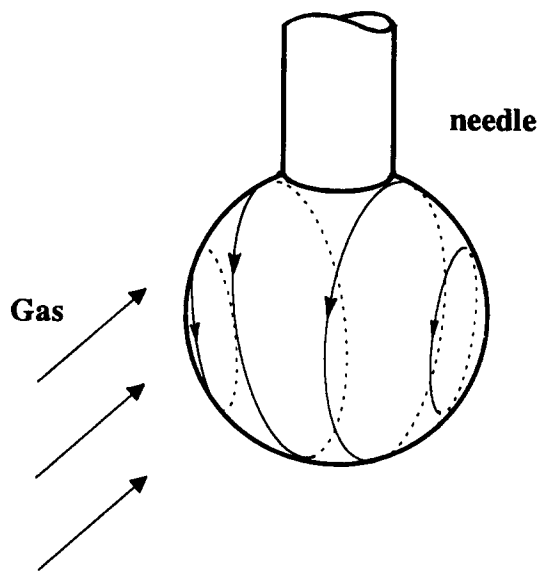

Figure 11 Liquid surface rotation pattern observed experimentally

between air and liquid near the top of the pendant droplet. In addition, there exist attractive capillary forces at the liquid–needle interface that oppose fluid flow. On the other hand, the gaseous stream flows over the lowest portion of the droplet in an unobstructed manner. Thus, the shear differential between the upper and lower portions of the droplet, as well as the "pinning" of the droplet at the liquid–needle interface, combine to maintain the experimentally observed surface rotational pattern (Figure 11). It should be noted that all experiments were performed at room temperature; therefore, the rate of liquid evaporation was low, and fluid properties were essentially constant. The droplet surface regression was intentionally suppressed to assure that the shear-induced liquid flow was not affected by the evaporative mechanisms.

A schematic of the experimental setup is presented in Figure 12. The droplet-suspending needle was mounted on a three-axis translation stage with a positioning accuracy of 2 μm. A steady flow of air was generated through a laminar flow device from which the gas flowed out horizontally (see Figure 12). The laminar flow device proved to be a critical component of the experimental setup, since steady reproducible flows were

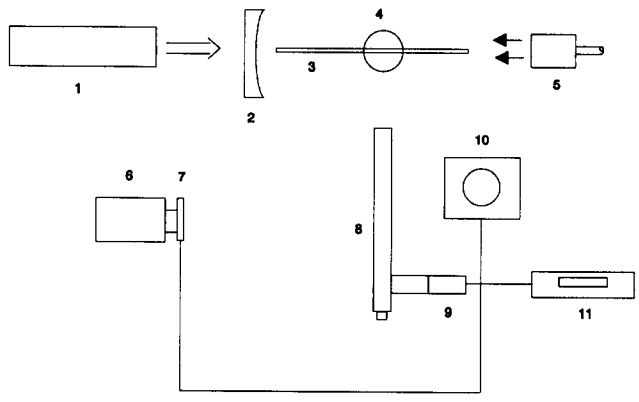

Figure 12 Suspended-droplet experimental setup: 1) CW Argon ion laser, 2) sheet-forming optics, 3) laser sheet, 4) suspended droplet, 5) laminar flow device, 6) computer, 7) frame grabber, 8) microscope, 9) video camera, 10) video monitor, 11) video cassette recorder

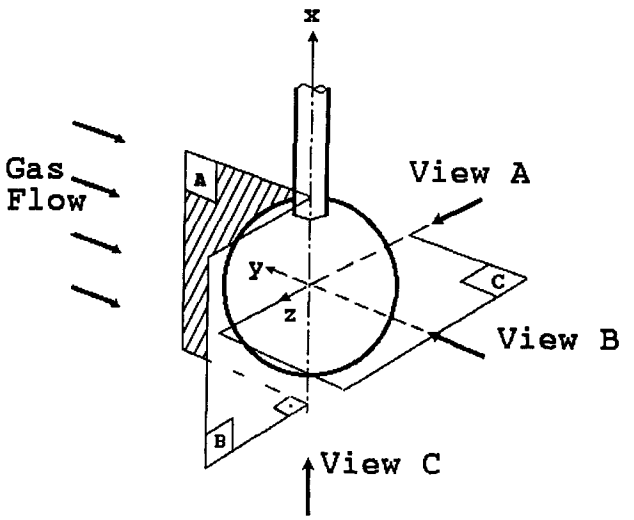

Figure 13 Experimental configuration for needle-suspended droplet internal flow visualization. The three mutually orthogonal orientations (A, B, and C) represent the laser slicing directions

necessary for adequate levels of repeatability. Metered air entered a cylindrical glass enclosure via a 5 mm i.d. tube that gradually tapered to an inside diameter of 33 mm. The entrance chamber of the device was followed by a porous plug, then a packed bed of 1 mm glass beads, a fine screen, a ceramic honeycomb with a cell density of 0.5 cell/mm^2, and finally a fine nylon mesh. The air flow to the device was regulated with a calibrated rotameter. Typical gas velocities employed were approximately 1 m/s. A hot-wire anemometer was used to determine the uniformity of the air stream emanating from the flow device. The velocities were measured with a grid spacing of the order of 4 mm. The velocity data indicated a temporally quiet flow (within 1 percent) with spatial uniformity well within 10 percent over the entire stream cross section.

The droplet was observed in real time through a microscope. Distilled water droplets of 2 mm in diameter were placed at the flat tip of the vertically-oriented 10 μL syringe (dimensions: 0.7 mm outer diameter; 0.1 mm inner diameter) and subsequently exposed to a steady air stream emanating from the laminar flow device. The flow device was oriented perpendicular to the syringe needle so that the resulting cross flow caused the droplet surface to rotate in the manner depicted in Figure 11. A seemingly steady motion was established within a second after exposure of the initially quiescent pendant droplet to the gaseous stream. The flow Reynolds numbers—based on droplet diameter as well as free-stream velocity and properties—were in the range from 100 to 130. Although suspended from the needle, the droplets were nearly spherical (typical aspect ratios around 0.9).

The droplet internal convective motion was visualized via planar, laser-induced fluorescence. Fluorescence signals were induced by laser excitation of a small mass of dilute aqueous laser dye solution (10^{-6}M rhodamine B/H_2O) that was occasionally introduced at the top of the suspended droplet by slightly depressing the syringe plunger. The addition of dye was estimated to alter the droplet mass by less than 1 percent at a time, so that the impact of dye injection on the internal droplet dynamics was minimal. Observation of dye-doped droplets without the external gas cross flow indicated that molecular diffusion of the dye under quiescent liquid conditions was negligibly slow.

Each droplet was illuminated by a thin laser sheet passing through its midplane at three mutually orthogonal orientations (see planes A, B, and C in Figure 13). Note that plane A coincides with the equatorial (x–y) plane of the droplet. The internal motion was visualized from three respectively perpendicular directions (views or perspectives A, B, and C; Figure 13). The fluorescent emission from the dye was used to follow the liquid-phase circulation and was recorded with a high spatial-resolution microscope and CCD camera/video recording system (see Figure 12).

A continuous-wave argon ion laser operated at a wavelength $\lambda = 514.5$ nm was used to excite the dye fluorescence. The laser sheet was produced by a set of spherical and cylindrical lenses preceding the droplet and had a $1/e^2$ thickness of the order of 100 μm. The sheet thickness was maintained over a longitudinal range of 3 mm. The receiving optics included an f/2.8 dual port long-distance microscope coupled to a black and white CCD video camera. A long-pass filter (with a cutoff at 530 nm) was placed in front of the microscope objective to suppress elastically scattered laser light from the droplet and needle. With a 5×-microscope objective placed 100 mm from the droplet, the linear magnification of the microscope was approximately 1.6:1 to yield a horizontal spatial resolution of 10.5 μm/pixel. For real-time data observation and storage, the video output of the camera was connected to a video monitor and recorded with a videocassette recorder. Once the events were recorded, individual frames of the videotape were digitized using a frame grabber/386 computer system. This digitization gave 8-bit gray-level images with dimensions of 512 columns by 480 lines.

Real-time observations performed on a series of water droplets showed distinct patterns of internal circulation throughout the range of Reynolds numbers examined. Since the water droplets vaporized within several minutes, the Reynolds number gradually decreased as a result of droplet size reduction. Our observations focused primarily on the early stages of droplet lifetime, during which the effect of the suspending needle is expected to be less important.

5. Flow visualization results

The internal motion of a series of pendant water droplets was observed using the fluorescence patterns, which traced the liquid flow for several seconds after each dye-injection event. As the dye was convected through the liquid medium, the fluorescence signal decayed due to dilution effects. The occasional transport of microscopic fluorescing tracer particles on the droplet surface provided an excellent means for following the liquid surface motion in real time. The surface rotation depicted in Figure 11 revealed a very repeatable pattern, particularly from perspective B of Figure 13. The angular frequency of this motion was measured with a timing device to be approximately 3 Hz, with a corresponding rotational Reynolds number around 0.2. This quantity, based on rotation velocity, droplet size, and free-stream properties, is frequently employed to characterize the intensity of rotation (Lozinski and Matalon 1992).

The droplet internal circulation was observed at different perspectives (A, B, or C of Figure 13), one viewing angle at a time. The consistency and reproducibility of the flow patterns were of primary concern. Reproducibility was needed to ensure that an accurate picture of the internal circulation was obtained by the nonsimultaneous observation of different sections of the droplets. It was found that the induced liquid motion was sensitive to the relative orientation of the suspended droplet with respect to the incoming air stream. This point was emphasized by the highly unstructured internal fluid motion obtained when the ambient flow was intentionally positioned

at nonorthogonal angles with respect to the axis of the suspended droplet. Conversely, with the droplet axis orthogonal to the air stream, the patterns observed for the shear-induced liquid flow showed excellent reproducibility over a series of tracing injections.

Three sequences of images are presented in Figure 14 for 2-mm droplets that were exposed to a uniform air stream of velocity 1 m/s and room temperature. The Reynolds number was 130, based on droplet diameter and free-stream properties. The three sequences correspond to perspectives A, B, and C illustrated in Figure 13. Note that each set displayed in Figure 14 corresponds to a unique injection event. Figure 14A presents a typical temporal variation of the fluorescence signal as observed from perspective A of Figure 13. In Figure 14A, the gaseous flow is directed from right to left and the needle is positioned at top of the droplet. The laser sheet was oriented vertically and passed through the droplet center in the direction of the ambient flow (x–y plane). The suspending needle is barely visible at the top of the droplet. Some background scattering from the laser sheet and the needle is indicated by two thin bright sections of the droplet surface located at either side of the needle near the top of the droplet. The images of Figure 14A reveal a spiral internal motion in that plane, in the clockwise direction, with a characteristic frequency that gradually increases as the dye approaches the center of the droplet. The timewise weakening of the intensity of the fluorescence signal, as shown in Figure 14A, was attributed to the gradual convection of dye away from the imaging (x–y) plane. Note that, in principle, the motion of the fluid located within the x–y plane should (by symmetry) be confined to that plane. Although the fluorescence signal did decay as the tracer dye continued to move towards the droplet center, a significant amount of dye remained on the slicing plane toward the end of the spiral. This suggests that the observed motion was nearly planar for perspective A and that the laser passed through the droplet center. The similarity between the flow-tracing path of Figure 14A and the model-predicted trajectory shown in Figure 10A suggests that the model captures a main feature of the droplet internal flow. This qualitative similarity exists even though the model neglects dependence on the azimuthal coordinate φ. The φ-dependence is probably present in the pendant droplet experiments.

The complex, 3-D, typical particle trajectory predicted by the model in Figure 9 (as applied to partially obstructed flow over a section of the droplet surface) was corroborated by the experimental observations. Specifically, when viewed from perspective B in real time, tracing dye particles could be followed as they swirled along the droplet surface, alternately

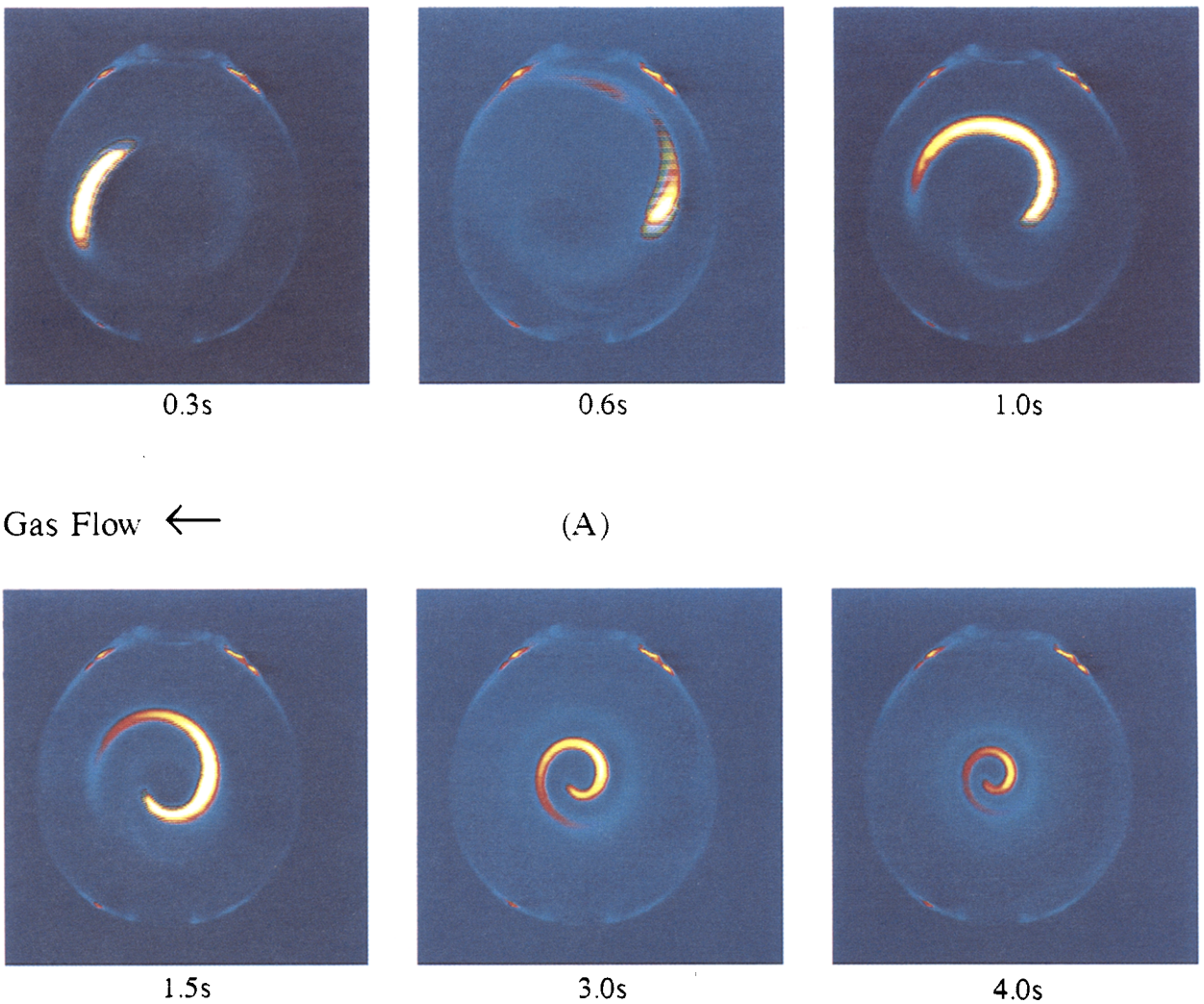

Figure 14 Transient fluorescence images for perspectives A, B, C displayed in Figure 13. The times after the onset of each dye injection event are shown beside each frame

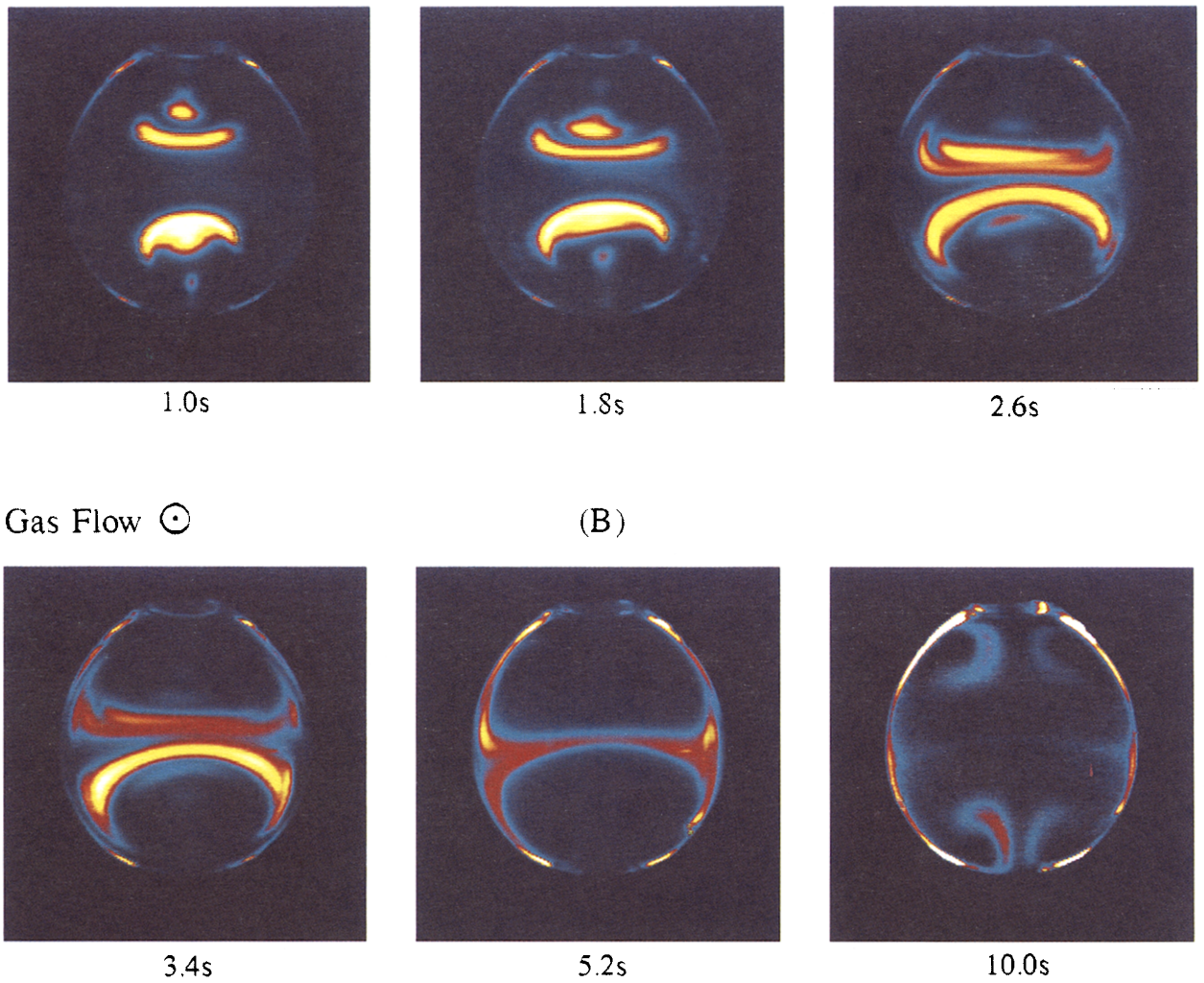

Figure 14 (continued)

moving in and out of the laser sheet. Each of these particles moved from the pole and along the droplet surface toward the equator whereupon it penetrated into the equatorial plane. In accord with Figure 9, each particle remained in this plane, since it could be seen to spiral inward toward the rotational axis. Once near the droplet center, the particle followed a helical path in the droplet interior, moving back toward the original pole and finally reappearing at the droplet surface. The rather striking similarity between numerical predictions and experimental observations provides support for the existence of 3-D trajectories such as the one depicted in Figure 9.

Figure 14B shows the temporal variation of the fluorescence signal during an injection event as observed from perspective B (see Figure 13). The air flow in that series is normal to the laser sheet, which coincides with the x–z plane of observation. The spiral motion displayed in Figure 14A was exhibited by a sequential flashing (in a temporal sense) of the fluorescent islands shown in the early frames of Figure 14B. As evidence of data consistency, we note that the characteristic frequency of the flashing events matched that of the spiral motion in perspective A. The planar images of Figure 14B appear nearly symmetric with respect to the vertical x-axis through the droplet center. The presence of the needle at the top of the droplet resulted in some minor asymmetry with respect to the horizontal axis (see intermediate frames of Figure 14B). Nevertheless, the overall dependence of the internal flow on the azimuthal coordinate φ appears to be minimal. The transport of dye reveals significant convective motion towards the droplet center and away from the vertical x–y plane that divides the liquid in the direction of the air flow. The quad-cell flow pattern clearly marked in the last frame of Figure 14B is consistent with the earlier tracer motion depicted in this sequence. This pattern also compares well with the model-predicted motion in that plane (Figure 10B), which neglects dependence on the azimuthal coordinate φ. Finally, it should be noted that the characteristic time for diffusion of the dye on plane B was at least an order of magnitude longer than that of the helical motion on plane A.

Figure 14C shows the temporal variation of the fluorescence signal during injection as observed from the bottom of the droplet (perspective C of Figure 13). The air flow in that series was directed from top to bottom. The laser sheet was oriented horizontally and passed through the droplet center. The similarity between the flow patterns of Figures 14B and 14C also suggests that the overall dependence of the internal flow on the azimuthal coordinate φ appears to be minimal. The close similarity between the observed flow in planes B and C thus validates one of the major assumptions of the numerical model (φ-independence).

The flow visualization images recorded by the video camera system and presented in Figure 14 were obtained by viewing the dye fluorescence through the droplet. Thus, as a result of

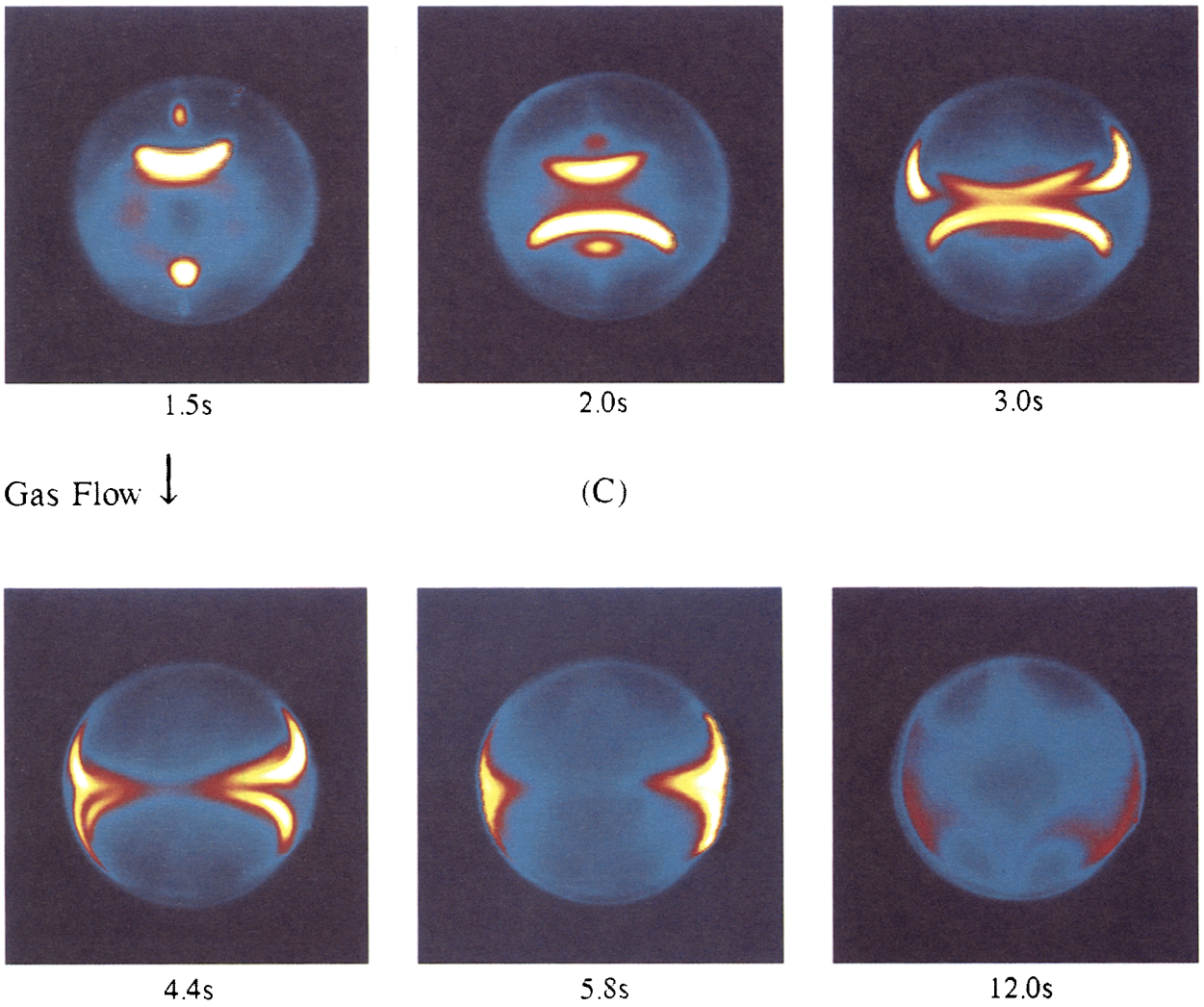

Figure 14 (continued)

light refraction at the droplet/air interface, geometric distortion of the fluorescence occurred in the camera image as described by Kintner et al. (1961), Benincasa et al. (1987), and Zhang and Melton (1994). Based on principles of geometrical optics, Kintner et al. have derived a simple expression for the distortion of an object point in the midplane of an ellipsoidal droplet. This relationship gives the conjugate image coordinates (as indicated by the camera image) as a function of the actual coordinates within the droplet midplane. Assuming the droplet to be spherical, the geometrical distortion is dependent only on the radial position. Furthermore, the coordinates of the image field are "stretched" radially outward relative to the actual radial coordinates. Using the aforementioned expression of Kintner et al. and assuming a spherical water droplet of refractive index 1.33, it was found that the radial stretch factor is constant for object coordinates up to 60 percent of the droplet radius. At larger radial coordinates, the distortion starts to decrease until the edge of the droplet, where no distortion occurs. From these results, we deduce that image restoration would alter only the length scales with no significant effects on the overall liquid flow behavior. Nor would there be any effect on the measured spiral period (as seen in plane A), since there is no distortion at the edge and center of the droplet.

6. Discussion

The typical fluid trajectory within the droplet, as shown in Figure 9, has been determined by the model using nonuniform droplet surface rotation. The selected circumferential velocity profile (Figure 6) mimics an obstructed rotation between two parallel planes located on either side of the x–y symmetry plane. The flow trajectory of Figure 9 is consistent with the flow visualization experiments, which suggest that tracing particles introduced near the top of the droplet undergo a spiral motion as they translate toward the center, and are subsequently convected away from the x–y plane of symmetry. The physical presence of the suspending needle at top of the droplet (Figure 11), however, suggests a model formulation that accounts for variation of the liquid velocities along the azimuthal (φ) direction. Our experimental observations consistently indicated that the magnitude of the azimuthal velocity component (w) was substantially larger than the magnitudes of the radial (u) and polar (v) velocity components (Figure 1). Therefore, the region most influenced by the needle consists of a strip of fluid that is moving on the droplet surface between two parallel vertical planes (P1, P2), as shown in Figure 1. The distance between these two planes is of the order of the needle diameter. The fluid particles moving on the droplet surface and within

the droplet strip in question are decelerated by the needle (no-slip condition). From that perspective, the azimuthal velocity component w on the droplet surface is expected to be lowest in the immediate vicinity of the needle and higher near the lowest portions of the suspended droplet. Given this physical picture, the w velocity component should be φ dependent. However, such a situation would require a 3-D modeling approach. The experimental observations clearly indicated that any azimuthal asymmetry induced by the needle is rather minimal (compare images of Figures 14B and 14C). Therefore, the relevant model assumption regarding symmetry along φ is well justified.

As a reasonable first-step approximation of the actual effect of the needle on the droplet internal motion, the needle-induced flow deceleration was accounted for by assuming the specific azimuthal velocity profile shown in Figure 6. In effect, the flow-retardation effect of the needle was assumed to be localized on the droplet surface between planes P1 and P2 of Figure 1. This approach preserved the azimuthal symmetry, yet allowed the retarding effect of the needle to be taken into account. It was found that the specific profile $w(\theta)$ did not influence the overall appearance of the internal flow (Figure 9), even though it did affect the respective ratios between characteristic transport times and lengths. The polar profile shown in Figure 6 was found to provide good agreement between characteristic transport times measured experimentally and those calculated by the model.

The above analysis and flow visualization experiments provide insight on the fluid transport processes within droplets that encounter ambient flows inducing transient of spatially nonuniform surface rotation. The relevant information has implications regarding the mixing efficiency and segregation of components in multicomponent droplets, energy transport rates, etc. The results indicate that the 3-D spiraling motion observed in rotating droplets, when present, critically alters the character of the single toroidal Hill's vortex established in axisymmetric flow configurations. To this end, the characteristic lengths of the relevant mixing processes are also affected. Since the characteristic times for mass diffusion and energy transport are inversely proportional to the square of the above characteristic length, it is concluded that processes involving droplet spinning may exhibit substantially different mixing times.

The fluid motion examined in the current study is qualitatively similar to that reported by Lozinski and Matalon (1993), even though the origin of the induced motion is fundamentally different for the two investigations (surface rotation vs. thermocapillary forces). It would be useful to quantitatively compare the internal circulation induced by variable surface tension, with the motion established due to transient of spatially nonuniform droplet surface rotation. Lozinski and Matalon's analysis is applicable in the limit of small values of the parameter $\Omega = R^2\omega/\alpha \ll 1$, where α is the gaseous thermal diffusivity. The parameter Ω represents the ratio of the droplet rotational velocity to the gaseous diffusion velocity. However, due to the room-temperature conditions employed in the current study, Ω is of the order of unity; therefore, a direct comparison is not possible.

7. Conclusions

This paper has presented a combined theoretical/experimental study of internal liquid circulation induced by droplet surface rotation. Such conditions may arise when a shear or locally rotating flow imposes a spinning motion on the droplet interface. The rotational frequencies considered were of the order of several Hertz, and correspond to low values of rotational Reynolds numbers. A numerical model was formulated to quantify the fluid transport within a droplet whose surface is subjected to specific modes of rotation about a central axis. The model predictions consistently showed that helical internal flows appear not only temporarily during the transient phases of spatially uniform surface-driven rotation, but may also develop at steady state as a result of spatial nonuniformities along the polar coordinate.

Planar laser-induced fluorescence was employed to provide high-resolution images of flow patterns developed within millimeter-sized pendant droplets. These droplets were exposed to steady laminar air streams at room temperature and atmospheric pressure. When the ambient flow was directed perpendicular to the needle–droplet axis, the droplet surface was observed to rotate at a seemingly steady angular velocity. The experimentally observed helical internal flow patterns were attributed to the flow-decelerating influence of the suspending needle, and showed good agreement with those predicted by the numerical model for ordered, spatially nonuniform surface rotation.

The revealed helical circulation patterns bear little resemblance to the widely studied 2-D toroidal internal flows established within droplets under axisymmetric conditions. These patterns are qualitatively similar to the ones induced by transient spinning or droplet interfacial temperature gradients, as reported by other investigators. The results showed that processes involving transient and/or spatially nonuniform shear-induced droplet rotation may exhibit substantially different liquid mixing rates compared to axisymmetric situations.

Acknowledgments

Useful discussions with Dr. Hratch Semerjian of NIST are acknowledged with appreciation. This work was sponsored in part by the Air Force Office of Scientific Research, Air Force Systems Command, USAF, under grant number AFOSR 92-J-0476. The U.S. Government is authorized to reproduce and distribute reprints for Governmental purposes notwithstanding any copyright notation thereon. The support of the NIST Scientific Computing Facility through an allocation of computer time on the Cray Y-MP is also acknowledged.

Notes

Commercial equipment identified herein does not imply recommendation by the National Institute of Standards and Technology, nor does it imply that this equipment is the best available for the purpose.

References

Benincasa, D. S., Barber, P. W., Zhang, J.-Z., Hsieh, W.-F., and Chang, R. K. 1987. Spatial distribution of the internal and near-field intensities of large cylindrical and spherical scatterers. *Appl. Optics*, **26**, 1348–1356

Chiang, C. H., Raju, M. S., and Sirignano, W. A. 1992. Numerical analysis of convecting, vaporizing fuel droplet with variable properties. *Int. J. Heat Mass Transfer*, **35**, 1307–1324

Dandy, D. S. and Leal, L. G. 1989. Buoyancy-driven motion of a deformable drop through a quiescent liquid at intermediate Reynolds numbers. *J. Fluid Mech.*, **208**, 161–192

Dayal, S. K., Srivastava, B. C., and Srivastava, N. K. 1971. Circulation patterns in charged and uncharged drops. *Indian J. Pure Appl. Phys.*, **9**, 195–196

Dukowicz, J. K. 1980. A particle–fluid numerical model for liquid sprays. *J. Comp. Phys.*, **35**, 229–253

Dwyer, H. A. 1989. Calculations of droplet dynamics in high temperature environments. *Prog. Energy Combust. Sci.*, **15**, 131–158

Eichhorn, R. and Small, S. 1964. Experiments on the lift and drag of spheres suspended in a Poiseuille flow. *J. Fluid Mech.*, **20**, 513–527

Faeth, G. M. 1983. Evaporation and combustion of sprays. *Prog. Energy Combust. Sci.*, **9**, 1–76

Ferziger, J. H. 1977. Large eddy numerical simulations of turbulent flows. *AIAA J.*, **15**, 1261–1267

Garner, F. H., Skelland, A. H. P., and Haycock, P. J. 1954. Speed of circulation in droplets. *Nature*, **173**, 1239

Hadamard, J. 1911. Mouvement permanent lent d'une sphere liquide et visquese dan un liquid viscqueux. *Com. Ren. de Sci. de l'Acad. de Sci.*, **152**, 1735–1738

Harriott, P. 1962. A review of mass transfer to interfaces. *Can. J. Chem. Eng.*, **40**, 60–69

Haywood, R. J., Nafziger, R., and Renksizbulut, M. 1989. A detailed examination of gas and liquid phase transient processes in convective droplet evaporation. *J. Heat Transfer*, **111**, 495–502

Hill, M. J. M. 1894. On a spherical vortex. *Phil. Trans. R. Soc.*, **185**, 213–245

Horton, T. J., Fritsch, J. R., and Kintner, R. C. 1965. Experimental determination of circulation velocities inside drops. *Can. J. Chem. Eng.*, **43**, 143–146

Kim, I., Elghobashi, S., and Sirignano, W. A. 1993. Three-dimensional flow over two spheres placed side-by-side. *J. Fluid Mech.*, **246**, 465–488

Kintner, R. C., Horton, T. J., Graumann, R. E., and Auberhar, S. 1961. Photography in bubble and drop research. *Can. J. Chem. Eng.*, **39**, 235–241

Law, C. K. 1982. Recent advances in droplet vaporization and combustion. *Prog. Energy Combust. Sci.*, **8**, 171–201

LeClair, B. P., Hamielec, A. E., Pruppacher, H. R., and Hall, W. D. 1972. A theoretical and experimental study of the internal circulation in water drops falling at terminal velocity in air. *J. Atmospher. Sci.*, **29**, 728–740

Lozinski, D. and Matalon, M. 1992. Vaporization of a spinning fuel droplet. *Proc. 24th Int. Symp. Combustion*, The Combustion Institute, Sydney, Australia, 1483–1491

Lozinski, D. and Matalon, M. 1993. Thermocapillary motion in a spinning vaporizing droplet. *Phys. Fluids A*, **5**, 1596–1601

McDonald, J. E. 1954. The shape and aerodynamics of large raindrops. *J. Meteor.*, **11**, 478–494

Megaridis, C. M. 1993. Comparison between experimental measurements and numerical predictions of internal temperature distributions of a droplet vaporizing under high-temperature convective conditions. *Comb. Flame*, **93**, 287–302

Natarajan, R. 1974. Some experimental observations of rotation, oscillation, spinning and swerving of falling burning drops. *Can. J. Chem. Eng.*, **52**, 834–837

Pearlman, H. G. and Sohrab, S. H. 1991. The role of droplet rotation in turbulent spray combustion modeling. *Combust. Sci. Technol.*, **76**, 321–334

Prakash, S. and Sirignano, W. A. 1980. Theory of convective droplet vaporization with unsteady heat transfer in the circulating liquid phase. *Int. J. Heat Mass Transfer*, **23**, 253–268

Pruppacher, H. R. and Beard, K. V. 1970. A wind tunnel investigation of the internal circulation and shape of water droplets falling at terminal velocity in air. *Q. J. R. Meteor. Soc.*, **96**, 247–256

Renksizbulut, M. and Haywood, R. J. 1988. Transient droplet evaporation with variable properties and internal circulation at intermediate Reynolds numbers. *Int. J. Multiphase Flow*, **14**, 189–202

Rybczinski, W. 1911. *Bull. Acad. Sci., Cracovie, Ser. A*, p. 40

Sarma, B. S. and Mondal, P. K. 1975. Spatial filtering techniques applied to internal flow visualization. *Indian J. Pure Appl. Phys.*, **13**, 97–98

Sirignano, W. A. 1983. Fuel droplet vaporization and spray combustion theory. *Prog. Energy Combust. Sci.*, **9**, 291–322

Sirignano, W. A. 1993. Fluid dynamics of sprays—1992 Freeman Scholar lecture. *J. Fluids Eng.*, **115**, 345–378

Spells, K. E. 1952. *Proc. Phys. Soc. (London)*, **B65**, 541–546

Wimmer, M. 1988. Viscous flows and instabilities near rotating bodies. *Prog. Aerospace Sci*, **25**, 43–103

Winter, M. 1993. Droplet slicing measurements of internal circulation. 31st Aerospace Sciences Meeting (Paper AIAA-93-0900), Reno, NV

Winter, M. and Melton, L. A. 1990. Measurement of internal circulation in droplets using laser-induced fluorescence. *Appl. Optics*, **29**, 4574–4577

Wong, S.-C. and Lin, A.-C. 1992. Internal temperature distributions of droplets vaporizing in high-temperature convective flows. *J. Fluid Mech.*, **237**, 671–687

Yung, C. N., De Witt, K. J., Brockwell, J. L., and Chai, A. T. 1991. The transient motion of a spherical fluid droplet. *Chem. Eng. Comm.*, **110**, 163–186

Zhang, J. and Melton, L. 1994. Numerical simulations and restorations of laser droplet-slicing images. *Appl. Optics*, **33**, 192–200